ROYAL SOCIETY
OF CHEMISTRY

PAPER

Check for updates

Filtration behavior and associated mechanisms of kaolinite and illite with emphasis on pH effect

Guolei Liu,[a] Xinde Xu,[a] Rongfeng Chen,[a] Huaizhi Shao, [ID] *[abc] Dongping Tao,[ab] Lu Yang[ab] and Xiangning Bu*[d]

The filterability and mechanisms of individual kaolinite and illite particles and their mixture have been investigated in aqueous solutions at different pH values by measuring the filtration rate and chord length distributions. The filtration rate decreased with pH values varying from 3 to 10, while the chord length distribution results showed that the clay mixture aggregated most significantly at pH 3. The particle interaction energy of the clay mixture, calculated according to the Derjaguin–Landau–Verwey–Overbeek (DLVO) theory, was determined to be attractive at pH 3. The pore size distribution (PSD) and porosity of the clay mixture filter cake were measured using the low-field nuclear magnetic resonance (LF-NMR) nanopore analyzer. The total porosity of the filter cake at pH 3 was higher than that at pH 10, leading to a higher filtration rate. It has been found from this study that the clay filterability depends on filter cake porosity, microstructure and the interaction of particles in the filter cake.

1 Introduction

Filtration is an essential process in mineral processing, used to recycle water and separate fine mineral particles from slurry.[1–3] It is worth noting that the filtration of fine tailings is always a major challenge. Many factors contribute to this challenge, including the size of particles, the ion composition in the process water, and the content and types of clays.[4–8] Among these factors, the fine clays present in the tailings play a key role in affecting dewatering efficiency.[9–11] Notably, kaolinite and illite minerals are the dominant forms of fine clays present in the tailings of coal washing and oil sands.[12] Many studies have focused on the effect of kaolinite or illite clay on the tailings treatment.[13–15] The role of illite clays in the tailings treatment was studied by Long *et al.*, and the results showed that illite particles could not coagulate in process water.[16] Li *et al.* investigated the filtration of kaolinite-coal mixture suspension and found that fine coal particles were trapped in the gaps of kaolinite flocs during filtration.[17] Wang *et al.* demonstrated the filterability of rutile, quartz, kaolinite, illite, illite–smectite and montmorillonite, and found that the primary factor affecting the dewatering of oil sands tailings was not the particle size of mineral but the type of mineral.[18] It should be mentioned that

the clay minerals contained in the tailings are generally a mixture of kaolinite and illite. It is not comprehensive to study the effect of a single kaolinite or illite clay on the tailings filtration. Compared to the effect of individual clay minerals on the filtration, the effect of interactions between mixed clays is much more complex.[19] Moreover, the filtration efficiency of clay minerals has been proven to be significantly affected by pH levels.[20,21] Shi *et al.* studied the interaction energy of a quartz and kaolinite system, indicating that the dewaterability of a quartz–kaolinite mixture in tailings was improved at pH 6.[22] However, few studies have investigated the effect of a kaolinite–illite mixture on the filtration process under varying solution pH values. Therefore, it is necessary to study the dewatering behavior of mixed clays in the filtration process and further reveal the interaction mechanisms of different clays in tailings.

In recent years, the low-field nuclear magnetic resonance (LF-NMR) technique has been well developed in the fields of porous media,[23,24] bitumen,[25,26] gas shale rocks,[27,28] clay minerals[29,30] and coal.[31,32] The basic principle of LF-NMR is to estimate the pore size distribution (PSD) by analyzing the water content in the pores. LF-NMR is regarded as a highly efficient and accurate method, especially for characterizing the pore wettability and PSD of porous minerals.[33–35] Mao *et al.* investigated the *in situ* water wetting of lignite pores using LF-NMR and reported that the mesopores and macropores on the lignite surface had a negative influence on lignite flotation.[31] He *et al.* studied the pore size distribution of coal by LF-NMR technique and demonstrated that this technique has the highest potential for PSD analysis due to its non-destructiveness and high accuracy.[24,32] It should be noted that combining LF-NMR pore analysis with DLVO theory to clarify the microstructure

[a]School of Resources and Environmental Engineering, Shandong University of Technology, Zibo, 255049, China. E-mail: shaohuaizhicumt@outlook.com

[b]Shandong Key Laboratory of Intelligent Magnetoelectric Equipment and Mineral Processing Technology, Weifang, 262600, China

[c]Xinwen Mining Group Company of Limited Liability, Taian, 271200, China

[d]Key Laboratory of Coal Processing and Efficient Utilization, China University of Mining and Technology, Ministry of Education, Xuzhou, 221116, China. E-mail: xiangning.bu@cumt.edu.cn

of mixed-clay filter cakes was a novel method. Moreover, focused beam reflectance measurement (FBRM) is a real-time particle-level observation method, which can record the size of particles in real time and observe the interaction between particles *in situ*.[36–38]

In this study, the dewatering behaviors of kaolinite, illite and their mixture in aqueous solutions at different pH values were investigated. The differences in filtration rates of kaolinite, illite and their mixture were explained in terms of the interaction energy of clay particles and the properties (the pore size distribution and the porosity of aggregates) of filter cake. Zeta potentials and chord length distributions of different clays were measured by Zetasizer Nano ZS and focused beam reflectance measurement (FBRM), respectively. The interaction energy of kaolinite, illite and their mixture was calculated according to the Derjaguin–Landau–Verwey–Overbeek (DLVO) theory. The pore size distribution (PSD) and the porosity of aggregates in the filter cake of mixed clay particles were obtained by the low-field nuclear magnetic resonance (LF-NMR) nanopore analyzer. This study provides an understanding of the filterability mechanisms of a kaolinite–illite clay mixture in the tailings treatment.

2 Experiment

2.1 Materials

Kaolinite and illite samples were purchased from Guangdong and Shanxi, China, respectively. The d_{50} of kaolinite and illite was about 10 μm and 45 μm, respectively, as measured using a Laser Particle Sizer (Bettersize-3000). The clay mixture was composed of 70% (by weight) kaolinite and 30% (by weight) illite, which represents a typical ratio for the clays in oil sands tailings.[39] Kaolinite (5 g), illite (5 g) and the mixed clay particles (3.5 g of kaolinite and 1.5 g of illite) were dispersed in 50 mL potassium chloride (10 mM) solutions, respectively. The suspensions of kaolinite, illite and mixed clays of different pH values (3, 6, 8 and 10) were prepared using hydrochloric acid and potassium hydroxide. Deionized water was used in this study.

2.2 Filtration tests

The filtration experiments were carried out with the suspensions of kaolinite, illite and mixed clays at pH 3, 6, 8 and 10 at a vacuum pressure of −0.1 MPa using the Buchner funnel filtration equipment as described in the literature.[17,40] The filtration time started upon the transfer of the suspension to the funnel and ended when the water on the filter cake surface disappeared. Each measurement was repeated three times to minimize the experimental errors. A 70 mm diameter filter paper of standard quality was used for the filtration tests. Filtration rate was used to evaluate the filterability of suspensions.[17] The equation is as follows:

$$u = \frac{V}{tA} = \frac{V}{t\pi R^2} \tag{1}$$

where u is the average filtration rate, m s^{-1}; V is the filtrate volume obtained after filtration, L; t is the filtration time, s; A is the effective filtration area, m^2; R is the radius of Buchner funnel, m.

2.3 Zeta potentials measurements

Zeta potentials of kaolinite, illite and mixed clays with varying pH values were analyzed by a Zetasizer Nano ZS (Malvern Instruments, U.K.). The suspensions (20 mL) of kaolinite, illite and mixed clays at different pH values were transferred into a cuvette by pipette to measure the zeta potentials. Each experiment was repeated five times to ensure the accuracy.

2.4 FBRM measurements

The chord lengths of kaolinite, illite and mixed clay particles in suspensions with varying pH values were measured by FBRM (G400, Mettler Toledo, USA), which can be used to evaluate the aggregation of particles. Samples of 0.5 g of kaolinite, illite and the mixed clays particles were dispersed in 400 mL of 10 mM KCl solutions, respectively. Then the three suspensions were adjusted to pH 3, 6 and 10, respectively. The FBRM probe was placed into the suspension to measure the chord length. The data of each test were collected with an impeller agitator rotating at 200 rpm. The FBRM results were analyzed using the mean diameter (d_{50}) and relative span (δ):[41]

$$\delta = \frac{d_{90} - d_{10}}{d_{50}} \tag{2}$$

where d_{90}, d_{10}, d_{50} are the droplet diameters corresponding to 90%, 10% and 50% (v/v) on cumulative curve. δ is used to characterize the emulsion dispersion; values less than 0.5 indicate a higher degree of monodispersity.

2.5 LF-NMR measurements

The LF-NMR nanopore analyzer (NMRC12-010V, China) was employed to analyze the PSD of aggregates by detecting the hydrogen atoms of the moisture in the pores among the particles. The filter cake samples of mixed clay particles obtained from the filtration experiments were used in the LF-NMR tests at a magnetic field intensity of 0.3 T and spectrometer frequency of 12 MHz with a 25 mm coil diameter probe. The echo time and the number of echoes were set at 0.3 ms and 16000, respectively. The sampling waiting time and the number of sampling times were 6000 ms and 32, respectively. The T_2 spectra of samples at pH 3 and 10 were obtained by the Carr–Purcell–Meiboom–Gill pulse sequence of LF-NMR.[31,34] The PSD and the porosity of aggregates were calculated using the LF-NMR analysis software according to the T_2 spectra.

3 Results and discussion

3.1 Filtration rate

Fig. 1 illustrates the filtration rate of kaolinite, illite and mixed clays in suspensions with varying pH values. With the increase in pH values, the filtration rate of kaolinite and illite decreased gradually. The filtration rate of illite decreased from 0.32 m s^{-1} at pH 3 to 0.27 m s^{-1} at pH 10, while the filtration rate of kaolinite was much lower. The filtration of mixed clays at
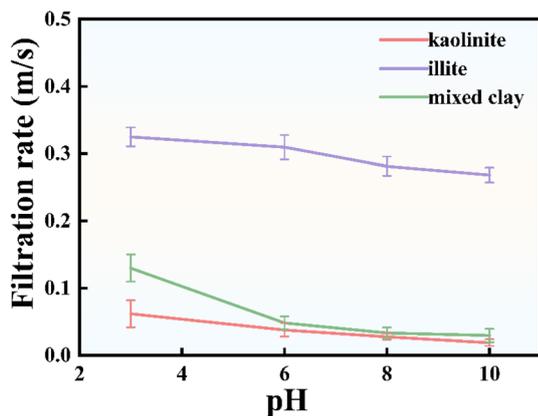
Fig. 1 Filtration rates of kaolinite, illite and mixed clays as a function of pH values.

Fig. 2 Zeta potentials of kaolinite, illite and mixed clays as a function of pH values.

pH 3 was much higher than at other pH values. In addition, the filtration rate of mixed clays was close to the rate of kaolinite, particularly from pH 6 to 10, which is probably because the content of kaolinite was much higher than that of illite in the mixed clays, indicating that the high content of kaolinite in the suspension leads to a high filtration resistance.[42,43] Although kaolinite constituted 70% of the mixed clays, its negative surface charge at pH 3 was neutralized by the positively charged illite particles, facilitating aggregation. This resulted in a more porous filter cake structure, which enhanced water permeability and the filtration rate. At higher pH, electrostatic repulsion between similarly charged particles led to dispersion and pore blockage, reducing filtration efficiency.

3.2 Zeta potentials of clay particles

Zeta potentials of kaolinite, illite and mixed clays are shown in Fig. 2 as a function of pH values. The negative values of zeta potentials of kaolinite particles increased with the increase in pH values, from approximately −15 mV at pH 3, −43 mV at pH 6 to −52 mV at pH 10, respectively. The values of illite zeta potentials changed from +10 mV at pH 2 to −42 mV at pH 10. The zeta potential of mixed clays approached zero at around pH 3, indicating its isoelectric point. The zeta potential curve of mixed clays was similar to that of illite particles from pH 2 to pH 6, but much closer to the kaolinite curve from pH 6 to pH 11. At pH 3, the negatively charged kaolinite particles would prefer to attach to the positively charged illite particles in the mixed suspension. The measured zeta potential of the mixed clays can be considered as a result of the combination of negatively charged kaolinite particles and weakly positively charged illite particles in the kaolinite-illite mixture. As the pH increased from 6 to 11, kaolinite and illite carried more negative charges. Thus, more and more kaolinite particles gradually detached from the surface of illite particles. Although some of the illite particles were exposed, the amount of exposed illite particles was significantly less than that of the fully exposed kaolinite particles, thus significantly increasing the influence of the negatively charged kaolinite on the zeta potential values of the mixed clays. Therefore, the zeta potential curve of the mixed
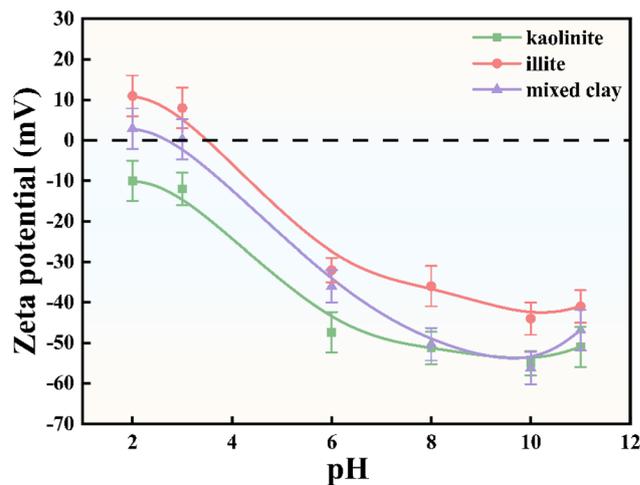
clays gradually approached the zeta potential values of kaolinite particles. Liu *et al.*[19] reported that the measured zeta potentials of a binary mixture depend on the interaction and the ratio of binary mixture. When there was an attraction between the binary mixture, the attachment would occur. Therefore, the ratio of mixture played an important role in determining the zeta potentials.

3.3 FBRM results

Calculated values of average diameters of the FBRM measurement results are given in Table 1. According to Table 1, the chord length distributions of illite, kaolinite and mixed clay particles in varying pH solutions are shown in Fig. 3. When aggregation occurred, the chord length value increased and the chord length distribution of particles was higher. In contrast, when the suspension was well dispersed, the measured chord length was closer to the natural size of the particles.[17,44] As shown in Fig. 3(a), the chord length of illite particles was concentrated in the range of 20 to 100 μm, while the chord length distribution at pH 3 was relatively higher in comparison with pH 6 and 10. Fig. 3(b) illustrates the chord length of kaolinite particles from pH 3 to 10. It shows that the particle size of kaolinite had no significant change from pH 3 to 10, indicating that the kaolinite suspension was well dispersed. This agrees well with the filtration rate results of kaolinite from pH 3 to 10, as shown in Fig. 1. The absence of significant aggregation in individual kaolinite or illite suspensions (Fig. 3(a) and (b)) was attributed to their similar surface charges under most pH conditions, leading to electrostatic repulsion. The aggregation observed in the mixed system at pH 3 was due to electrostatic attraction between oppositely charged particles. In Fig. 3(c), the peak at pH 3 on the distribution curve shifted to a significantly larger chord length. Since self-aggregation of kaolinite and illite was not obvious, the fact that the chord length became significantly larger at pH 3 in the mixture indicates that the aggregates in mixed clays were dominant. Thus, the mixed clays aggregated more significantly at pH 3, while the

Table 1 Average diameters (d_{10}, d_{50}, d_{90}, and δ) of illite, kaolinite and illite–kaolinite mixture[a]

Parameter (μm)	Illite			Kaolinite			Illite–kaolinite mixture		
	pH 3	pH 6	pH 10	pH 3	pH 6	pH 10	pH 3	pH 6	pH 10
d_{10}	23.84 ± 2.25	19.56 ± 1.14	20.90 ± 0.57	2.35 ± 0.06	1.96 ± 0.10	1.69 ± 0.16	22.97 ± 1.33	13.27 ± 0.36	13.60 ± 0.70
d_{50}	44.56 ± 3.40	35.42 ± 3.53	36.66 ± 2.71	4.79 ± 0.19	3.83 ± 0.28	3.38 ± 0.26	45.47 ± 4.53	24.90 ± 1.84	25.74 ± 1.86
d_{90}	84.15 ± 2.16	64.91 ± 1.32	63.57 ± 2.76	16.27 ± 0.24	13.03 ± 0.34	10.24 ± 0.26	96.18 ± 1.95	57.44 ± 2.50	55.09 ± 1.43
δ	1.35 ± 0.09	1.28 ± 0.08	1.16 ± 0.06	2.91 ± 0.08	2.89 ± 0.14	2.53 ± 0.17	1.61 ± 0.10	1.77 ± 0.09	1.61 ± 0.08

[a] $a1 \pm a2$ – $a1$ and $a2$ are the average and the standard deviation values of the measured data.

chord length of mixed clays showed no obvious difference at pH 6 and 10.

3.4 Interaction energy of clay particles

Many researchers have reported that the interaction energy between clay particles based on the DLVO theory includes contributions from the electrostatic double layer (edl) and the van der Waals (vdW) forces.[9,44,45] The interaction energy models of two spherical particles are given below:[46,47]

$$E_{\text{Total}} = E_{\text{vdW}} + E_{\text{edl}} \tag{3}$$

$$E_{\text{edl}} = \frac{\pi\varepsilon\varepsilon_0 R_1 R_2}{R_1 + R_2}\left(\varphi_1^2 + \varphi_2^2\right)\left[2\frac{\varphi_1\varphi_2}{\varphi_1^2 + \varphi_2^2}\ln\frac{1 + e^{-\kappa h}}{1 - e^{-\kappa h}}\right.$$
$$\left. + \ln\left(1 - e^{-2\kappa h}\right)\right] \tag{4}$$

where φ_1 and φ_2 are the surface potentials of kaolinite and illite, which are substituted by the measured zeta potential values; ε_0 is the permittivity of vacuum; ε is the dielectric constant of the solution; κ^{-1} is the Debye length, given as follows:

$$\kappa^{-1} = 0.304\left/\sqrt{C}\right. \tag{5}$$

where C is the concentration of the electrolyte, with a value of 0.01 mol L^{-1} in this work.

$$E_{\text{vdW}} = -\frac{A_{132}}{6h}\frac{R_1 R_2}{R_1 + R_2} \tag{6}$$

$$A_{132} \approx \left(\sqrt{A_{11}} - \sqrt{A_{33}}\right) \times \left(\sqrt{A_{22}} - \sqrt{A_{33}}\right) \tag{7}$$

where A_{132} refers to the Hamaker constant of clay minerals in aqueous media; the clay particles were considered as spherical,
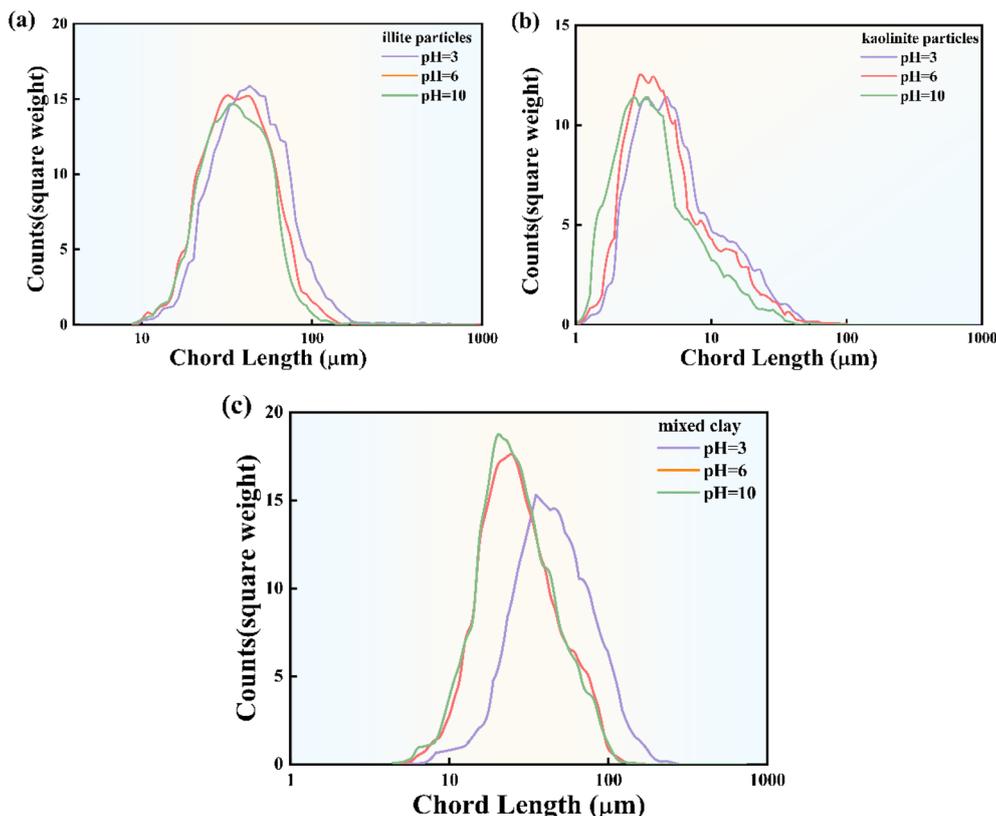

Fig. 3 Chord length distributions of illite (a), kaolinite (b) and mixed clay particles (c) in varying pH solutions.
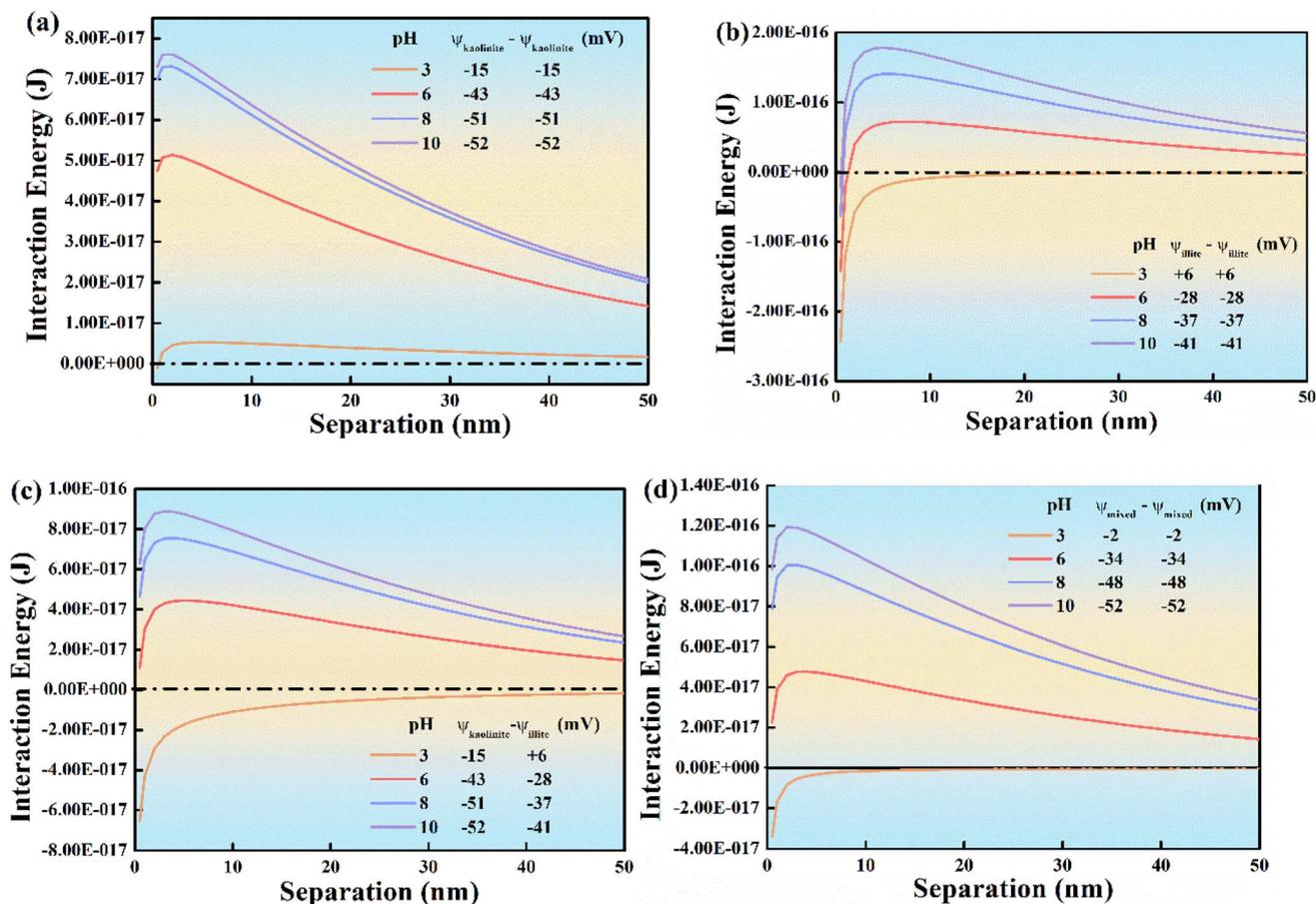
Fig. 4 Interaction energy between kaolinite particles (a), illite particles (b), kaolinite and illite particles (c), and mixed clay particles (d).

and R_1 and R_2 refer to the radii of two spherical kaolinite and illite particles; h is the distance between the clay surfaces. The Hamaker constants of kaolinite, water, and illite are 6.8×10^{-20} J, 3.7×10^{-20} J, and 1.40×10^{-19} J, respectively.[48,49]

Fig. 4 shows the interaction energy between different particles according to the DLVO theory. As shown in Fig. 4(a), the repulsive interaction energy between kaolinite particles increases from pH 6 to 10, indicating that the kaolinite particles are dispersed well in different pH solutions. This is consistent with the FBRM results of kaolinite suspension in Fig. 3(b). Although the zeta potential of the whole particle is negative and thus the Si-basal plane is negatively charged, the Al-basal plane and the edge surfaces are positively charged according to Chang's study,[50] due to the lamellar structure and anisotropy of kaolinite, and thus kaolinite particles would aggregate and form large and loose aggregates with a card-house structure, leading to a slightly higher filtration rate of kaolinite suspension at pH 3.

The interaction energy between illite particles was repulsive from pH 6 to 10. However, it became attractive at pH 3, as can be seen in Fig. 4(b). Therefore, the illite particles aggregated at pH 3 due to this attractive interaction, and the aggregates in the illite suspension at pH 3 were observed by FBRM in Fig. 3(a). Fig. 4(c) shows the interaction energy between kaolinite and

illite particles, according to the zeta potential values of each particle in the corresponding solution. There was an attractive interaction at pH 3 because of the opposite charges of kaolinite and illite particles. With increasing pH values, the attractive interaction reversed to repulsion and increased gradually. In Fig. 4(d), the interaction energy of mixed particles was calculated using the zeta potentials of mixed particles measured in different pH solutions. The interaction of mixed particles was attractive at pH 3, thus the illite particles were covered by smaller kaolinite particles. The electrostatic attraction of mixed particles changed to repulsion at pH 6, meaning that more and more kaolinite particles separated from the surface of illite particles, leading to the loosening of the aggregation. The repulsive interaction facilitated the dispersion of mixed particles with increasing pH values.

It should be noted that the calculated interaction of kaolinite and illite particles showed a similar trend with the interaction of mixed particles, suggesting the measured zeta potential values of mixed particles were reasonable and reliable. However, the attraction of mixed particles at pH 3 in Fig. 4(d) was obviously smaller than that between kaolinite and illite shown in Fig. 4(c). The main reason lies in that the zeta potential values used in the calculation were obtained from different suspensions. The zeta potentials used in Fig. 4(c) were

obtained from kaolinite and illite, respectively, while the zeta potentials of mixed particles were the total potentials of the mixture. Due to the aggregates in the mixture suspension at pH 3, the zeta potential values were different. The larger the difference in Fig. 4(c) and (d), the more significant was the aggregation in the mixed clay suspension.

3.5 Filtration performance of mixed clays

Fig. 5 shows the variation of the filtration time-to-volume ratio with filtrate volume of mixed clay at pH 3 and 10. The slope k and intercept b are obtained from the straight lines fitting with the data. Combined with Darcy's law, Carman–Kozeny equation and Svarovsky's modified formula, the filter medium resistance R_m and specific cake resistance α can be calculated,[51,52] as shown in eqn (8).

$$\frac{t}{V} = \frac{\alpha \mu c}{2A^2 \Delta P} V + \frac{R_m \mu}{A^2 \Delta P} \tag{8}$$

where, V is the filtration volume corresponding to the filtration time t, mL; A is the cake area, m²; ΔP is the differential pressure of the pressurized filter tank, N m⁻²; c is pulp mass concentration, kg m⁻³; μ is the absolute viscosity of water, N s m⁻². Here, A is 0.0104 m², ΔP is 100000 N m⁻², c is 100 kg m⁻³, and μ is 0.001 N s m⁻².

The results of the specific cake resistance (α) and medium resistance (R_m) of mixed clay at pH 3 and 10 are shown in Table 2. At pH 3, both the specific cake resistance and medium resistance were significantly lower than those at pH 10, increasing from 1.1032 m kg⁻¹ and 2926.8 m⁻¹ to 1.4926 m kg⁻¹

and 6324.1 m⁻¹, respectively. This indicates that the solution pH exerted a pronounced influence on filtration performance, which was associated with the aggregation behavior of kaolinite and illite particles.

The PSD and porosity of aggregates at pH 3 and 10 in the filter cake of mixed clay particles measured by LF-NMR are illustrated in Fig. 6. As shown in Fig. 6(a) and (c), the PSD of aggregates at pH 3 was higher than that at pH 10, while there was an obvious peak between 0.001 and 0.01 μm pore size at pH 3. This demonstrated that there were not only more mesopores (0.1–1 μm) but also more micropores (10^{-3} to 10^{-2} μm) at pH 3 than at pH 10.[53,54] Fig. 6(b) and (d) show that the pore size at pH 10 was mainly in the range of 0.10–0.40 μm, while the pore size at pH 3 mainly consisted of 0.16–0.63 μm particles. Thus, the mesopores played a dominant role in the pores of aggregates at pH 3 and 10. The broader pore size distribution at pH 3 (0.16–0.63 μm) was attributed to the formation of large aggregates, which created more mesopores. In contrast, at pH 10, the dispersed fine particles occupied inter-particle spaces, leading to a narrower pore size distribution (0.10–0.40 μm) and reduced overall porosity. Besides, there were no macropores (>1 μm) in the filter cake of mixed clay particles. Furthermore, the total porosity of aggregates was 66.86% at pH 3, which was higher than that at pH 10 (55.38%). Therefore, the filter cake at pH 3 had a higher filtration rate due to the larger porosity of aggregates, which was caused by the capillary effect of water in the large pores.[55,56]

3.6 Mechanisms

Fig. 7 shows the schematic diagram of the interaction of mixed clays in suspension and the filtration behavior of mixed clays in the filter cake at pH 3 and pH 10, respectively. For mixed illite and kaolinite systems, the interaction between illite and kaolinite determined the filtration rate in different pH solutions, as shown in Fig. 7(a) and (b). Fig. 7(a) and (b) illustrate that some fine particles might still form loose aggregates even at pH 10 due to van der Waals forces or mechanical entrapment, though electrostatic repulsion dominated. This minor aggregation did not significantly enhance porosity compared to the large, structured aggregates formed at pH 3. The attractive interaction between illite and kaolinite particles induced aggregate formation, resulting in an enlarged gap of the filter cake. These coarser pore channels facilitated enhanced water flow, thereby accounting for the higher filtration rate observed at pH 3, as shown in Fig. 7(c). The enhancement of porosity through the aggregation of fine particles has also been reported by other researchers.[57,58] With the increase in pH, the number of free fine kaolinite particles in the suspension increased, which was confirmed by FBRM measurements. This increase in dispersed fine kaolinite particles in suspension led to the blockage of the filter cake gap, which had a negative effect on water removal during filtration. While FBRM effectively indicated the presence of larger aggregates at pH 3 through increased chord lengths, it is noteworthy that this technique does not differentiate between the morphologies of aggregates, such as loose, open structures *versus* dense, compact ones.
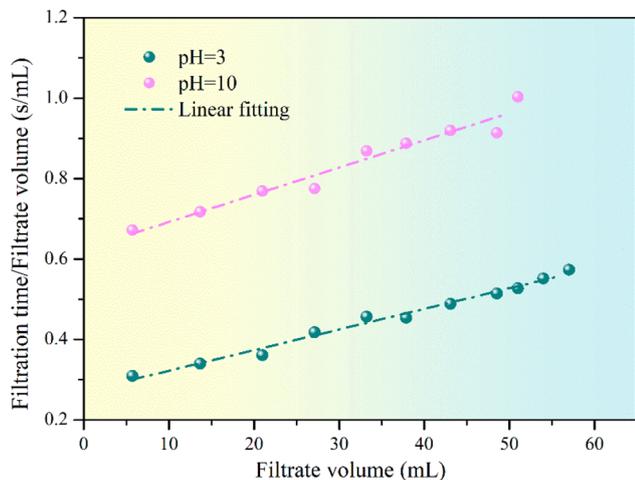

Fig. 5 Variation of the filtration time-to-volume ratio with filtrate volume of mixed clay at pH 3 and 10.

Table 2 Results of specific cake resistance (α) and medium resistance (R_m)

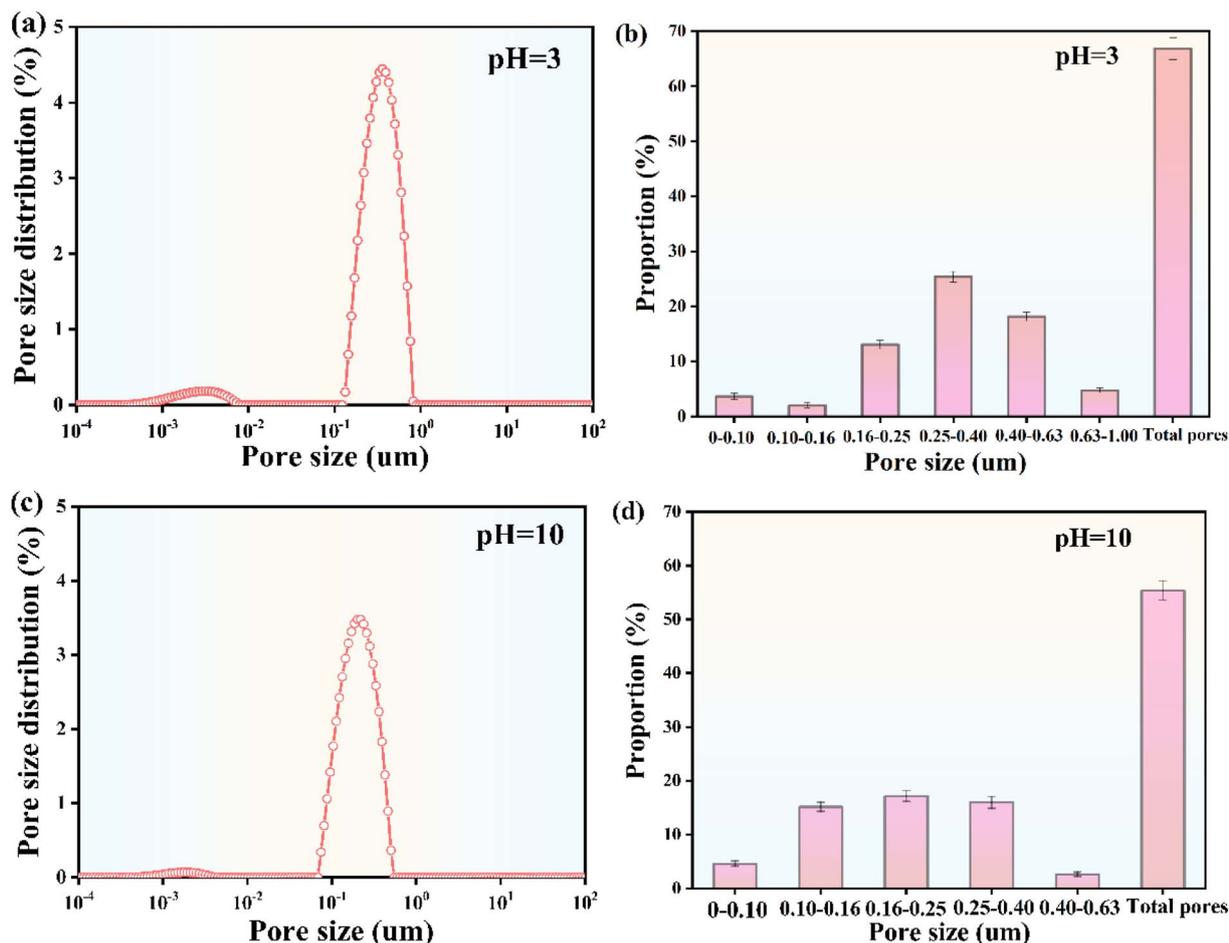| Test	Fitting equations	α/m kg⁻¹	R_m/m⁻¹
pH 3	$y = 0.0051x + 0.2706$	1.1032	2926.8
pH 10	$y = 0.0069x + 0.5847$	1.4926	6324.1

Fig. 6 PSD and porosity of aggregates in the filter cake of mixed clay at pH 3 (a) and (b) and pH 10 (c) and (d).
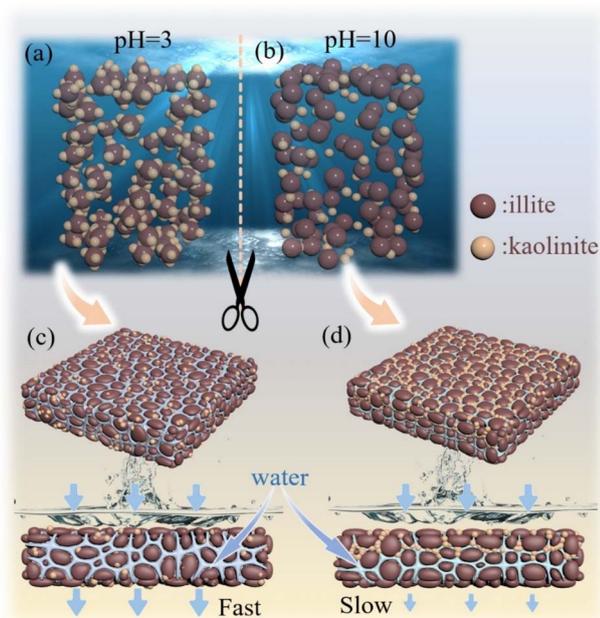

Fig. 7 Schematic illustration of the interaction of mixed clays in suspension at pH 3 (a) and pH 10 (b), and the filtration behavior of mixed clays in the filter cake at pH 3 (c) and pH 10 (d).

Complementary imaging techniques, such as scanning or transmission electron microscopy (SEM/TEM), would be highly beneficial in future work to visually characterize the microstructure of these aggregates and provide a direct link between the interaction energy, the macroscopic filtration properties, and the microstructural arrangement of particles within the filter cake.

Furthermore, dispersed kaolinite particles accumulated at the surface of the filter cake at pH 10, forming a compact sludge layer that significantly impaired filtration efficiency,[59] as depicted in Fig. 7(d). Thus, the particle size of clay had a significant effect on the filtration process. The suspended fine particles of kaolinite tended to block the gaps in the filter cake in the filtration process, resulting in a dense layer on the top of the cake, which was not conducive to the removal of water from the filter cake. Larger clay particles and aggregates could be filtered more easily, because more large gaps were generated in the cake, which helped to remove water from the filter cake quickly.

4 Conclusions

In this study, the filterability of kaolinite, illite and mixed clays in different pH solutions was investigated by measuring the

filtration rate, zeta potential, chord length distributions, interaction energy and pore size. Filtration rates of kaolinite, illite, and mixed clays decreased progressively with increasing pH, though mixed clays exhibited significantly enhanced filtration at pH 3 compared to other pH conditions. Filtration rates in mixed clays were controlled by interactions between kaolinite and illite particles. Filter cakes formed at pH 3 demonstrated substantially higher porosity and filtration rates than those at pH 10, confirming a critical link between cake microstructure and dewatering performance. Fine kaolinite particles impeded filtration by blocking filter cake pores and forming a dense surface layer, whereas larger particles/aggregates enhanced filtration performance by creating more permeable pathways within the cake structure that facilitated rapid water removal. This study clarified pH-dependent filtration mechanisms of clay mixtures in a monovalent electrolyte simplified system. Real tailings contain multivalent ions and organics that may alter these behaviors. Our future work will address these complex conditions to better simulate industrial conditions and improve industrial relevance.

Author contributions

Guolei Liu: writing – original draft, methodology, funding acquisition, data curation, conceptualization. Xinde Xu: visualization, investigation, data curation. Rongfeng Chen: investigation, formal analysis, conceptualization. Dongping Tao, Lu Yang: validation, project administration, methodology, investigation. Huaizhi Shao, Xiangning Bu: writing – review & editing, writing – original draft, validation, methodology, funding acquisition, data curation.

Conflicts of interest

The authors declare no conflict of interest.

Data availability

Data will be made available upon request.

Acknowledgements

References

1 R. Hogg, *Int. J. Miner. Process.*, 2000, **58**, 223–236.
2 D. Tao, J. G. Groppo and B. K. Parekh, *Miner. Eng.*, 2000, **13**, 163–171.
3 D. Tao, B. K. Parekh, J. T. Liu and S. Chen, *Int. J. Miner. Process.*, 2003, **70**, 235–249.
4 N. Alam, O. Ozdemir, M. A. Hampton and A. V. Nguyen, *Fuel*, 2011, **90**, 26–35.
5 E. Sabah, H. Yüzer and M. S. Çelik, *Int. J. Miner. Process.*, 2004, **74**, 303–315.
6 E. Sabah and Z. E. Erkan, *Fuel*, 2006, **85**, 350–359.
7 H. Shao, J. Chang, Z. Lu, B. Luo, J. S. Grundy, G. Xie, Z. Xu and Q. Liu, *Langmuir*, 2019, **35**, 6532–6539.
8 D. Tao, J. G. Groppo and B. K. Parekh, *Coal Prep.*, 1999, **20**, 207–225.
9 Y. Yu, L. Ma, H. Xu, X. Sun, Z. Zhang and G. Ye, *Powder Technol.*, 2018, **330**, 147–151.
10 A. Doi, M. Ejtemaei and A. V. Nguyen, *Miner. Eng.*, 2019, **143**, 105929.
11 D. Liu, M. Edraki and L. Berry, *Powder Technol.*, 2018, **326**, 228–236.
12 J. H. Masliyah, Z. Xu and J. A. Czarnecki, *Handbook on theory and practice of bitumen recovery from Athabasca oil sands*, Kingsley Knowledge Pub., 2011.
13 H. Shao, J. Chang, Z. Lu, J. S. Grundy, G. Xie, Z. Xu and Q. Liu, *J. Phys. Chem. C*, 2020, **124**, 2079–2087.
14 X. Ding, C. Repka, Z. Xu and J. Masliyah, *Can. J. Chem. Eng.*, 2006, **84**, 643–650.
15 M. Zhang, P. Li, W. Yao, Z. Xu and R. Fan, *Colloids Surf., A*, 2022, **638**, 128296.
16 J. Long, Z. Xu and J. H. Masliyah, *Colloids Surf., A*, 2006, **281**, 202–214.
17 Y. Li, W. Xia, B. Wen and G. Xie, *J. Colloid Interface Sci.*, 2019, **555**, 731–739.
18 D. Wang, H. Tao, K. Wang, X. Tan and Q. Liu, *Fuel*, 2022, **316**, 123395.
19 J. Liu, Z. Zhou, Z. Xu and J. Masliyah, *J. Colloid Interface Sci.*, 2002, **252**, 409–418.
20 R. Chen, Y. Fan, X. Dong, X. Ma, Z. Feng, M. Chang and N. Li, *Colloids Surf., A*, 2021, **622**, 126698.
21 L. Liang, L. Wang, A. V. Nguyen and G. Xie, *Powder Technol.*, 2017, **309**, 1–12.
22 Z. Shi, B. Ran and L. Liu, *Powder Technol.*, 2022, **409**, 117842.
23 J. Zhan, P. Zhang, Y. Wang and Q. Wu, *Chem. Eng. Sci.*, 2021, **244**, 116804.
24 L. Chen, D. J. McClements, Y. Ma, T. Yang, F. Ren, Y. Tian and Z. Jin, *Int. J. Biol. Macromol.*, 2021, **173**, 307–314.
25 K. Yang, P. R. J. Connolly, M. Li, S. J. Seltzer, D. K. McCarty, M. Mahmoud, A. El-Husseiny, E. F. May and M. L. Johns, *J. Pet. Sci. Eng.*, 2020, **195**, 107847.
26 O. Serve, H. Choblet, V. Livadaris and J.-P. Korb, *J. Colloid Interface Sci.*, 2021, **593**, 21–31.
27 G. Zhou, Z. Gu, Z. Hu, J. Chang, X. Duan, X. Liu, Y. Li and H. Zhan, *J. Pet. Sci. Eng.*, 2020, **195**, 107926.
28 G. Zhao and C. Wang, *Fuel*, 2019, **238**, 51–58.
29 X. Guichet, M. Fleury and E. Kohler, *J. Colloid Interface Sci.*, 2008, **327**, 84–93.
30 P. Conte, C. Abbate, A. Baglieri, M. Nègre, C. De Pasquale, G. Alonzo and M. Gennari, *Org. Geochem.*, 2011, **42**, 972–977.
31 Y. Mao, W. Xia, Y. Peng and G. Xie, *Fuel*, 2020, **272**, 117737.
32 Q. He, Y. Cao, Z. Miao, X. Ren and J. Chen, *Energy Fuels*, 2017, **31**, 13259–13265.
33 Y. Yao and D. Liu, *Fuel*, 2012, **95**, 152–158.
34 Y. Mao, Q. Li, W. Xia, Y. Li, G. Xie and Y. Peng, *Powder Technol.*, 2020, **375**, 445–452.

35 Y. Mao, W. Xia, G. Xie and Y. Peng, *Measurement*, 2020, **155**, 107564.

36 X. Wang, S. Zhou, X. Bu, C. Ni, G. Xie and Y. Peng, *Sep. Sci. Technol.*, 2021, **56**, 1418–1430.

37 S. Sankaranarayanan, B. Likozar and R. Navia, *Sci. Rep.*, 2019, **9**, 10126.

38 Z. Shi, Z. Yang, Z. Wang and L. Liu, *Sep. Purif. Technol.*, 2024, **332**, 125773.

39 J. H. Masliyah, J. Czarnecki and Z. Xu, *Handbook on theory and practice of bitumen recovery from Athabasca oil sands - Volume 1: Theoretical basis*, 2011.

40 Y. Fan and X. Dong, *Energy Technol.*, 2015, **3**, 1084–1092.

41 J. Gao, X. Bu, S. Zhou, X. Wang, M. Bilal, F. U. Hassan, A. Hassanzadeh, G. Xie and S. C. Chelgani, *Ultrason. Sonochem.*, 2022, **83**, 105928.

42 Y. Li, Y. Chen, W. Xia and G. Xie, *Powder Technol.*, 2021, **381**, 122–128.

43 X. Ma, Y. Fan, X. Dong, R. Chen, H. Li, D. Sun and S. Yao, *Minerals*, 2018, **8**, 400.

44 Y. Yu, G. Cheng, L. Ma, G. Huang, L. Wu and H. Xu, *Powder Technol.*, 2017, **313**, 122–128.

45 L. Liang, L. Wang, A. V. Nguyen and G. Xie, *Powder Technol.*, 2017, **309**, 1–12.

46 A. V Nguyen, H. J. Schulze, A. V. Nguyen and H. J. Schulze, *Colloidal Science of Flotation*, 2004, **118**, 1–850.

47 J. N. Israelachvili, *Intermolecular and Surface Forces*, 3rd edn, 2011.

48 V. Gupta and J. D. Miller, *J. Colloid Interface Sci.*, 2010, **344**, 362–371.

49 B. E. Novich, *Clays Clay Miner.*, 1984, **32**, 400–406.

50 J. Chang, H. Shao, B. Liu, R. Manica, Z. Li, Q. Liu and Z. Xu, *J. Colloid Interface Sci.*, 2021, **582**, 439–445.

51 P. Hu, L. Liang, W. Wang, Y. Li and G. Xie, *Energy Sources, Part A*, 2020, **46**, 14726–14738.

52 L. Svarovsky, *Solid-Liq. Sep.*, 2001, 302–334.

53 B. B. Hodot, *Outburst of coal and coalbed gas (Chinese Translation*, China Coal Industry Press, Beijing, 1966, p. 318.

54 M. Zou, C. Wei, M. Zhang, J. Shen, Y. Chen and Y. Qi, *Energy Fuels*, 2013, **27**, 3699–3708.

55 J. Addai-Mensah, *Powder Technol.*, 2007, **179**, 73–78.

56 C. L. Lin and J. D. Miller, *Chem. Eng. J.*, 2000, **80**, 221–231.

57 S. Zhou, X. Bu, M. Alheshibri, H. Zhan and G. Xie, *Chem. Eng. Commun.*, 2021, 1–11.

58 G. Xu, L. Liu, D. Geng, H. Shao, H. Wang, D. Tao, Z. Liu and M. Bilal, *Int. J. Coal Prep. Util.*, 2025, DOI: **10.1080/19392699.2025.2492718**.

59 M. Le Roux, Q. P. Campbell, M. S. Watermeyer and S. De Oliveira, *Miner. Eng.*, 2005, **18**, 931–934.